# Fabrication of PLLA/HA composite scaffolds modified by DNA

Yuki Nishida [a], Ryota Domura [a], Reika Sakai [a], Masami Okamoto [a, *], Shuichi Arakawa [a], Ryoji Ishiki [b], Max R. Salick [c], Lih-Sheng Turng [d]

[a] Advanced Polymeric Nanostructured Materials Engineering, Graduate School of Engineering, Toyota Technological Institute, 2-12-1 Hisakata, Tempaku, Nagoya 468 8511, Japan
[b] Medical Affairs, Toyota Technological Institute, 2-12-1 Hisakata, Tempaku, Nagoya 468-8511, Japan
[c] Department of Engineering Physics, University of Wisconsin—Madison, WI, USA
[d] Wisconsin Institute for Discovery and Polymer Engineering Center, Department of Mechanical Engineering, University of Wisconsin—Madison, WI, USA

## ARTICLE INFO

## ABSTRACT

Poly-L-lactide (PLLA)/natural hydroxyapatite (n-HA) composite scaffolds with different morphology and porosity were prepared using thermally induced phase separation (TIPS) technique. The morphological features of the scaffolds were observed by field emission scanning electron microscope (FE-SEM). The solvent concentration had much effect on the porosity and pore morphology. The double-stranded deoxyribonucleic acid (ds-DNA) adsorption behavior was investigating with the aim of their applications in gene therapy. The propensity of the scaffolds and n-HA particles to adsorb ds-DNA was assessed by batch experiments at pH 4. The aggregated size of the ds-DNA molecules and agglomeration after adsorption were characterized by dynamic light scattering (DLS) and Fourier transform infrared (FTIR) spectroscopic imaging.

The adsorption data were fitted into the Freundlich equation and the adsorption parameters were assessed. Although the adsorption capacity of the scaffolds was lower as compared to n-HA particles, it was sufficient for ds-DNA adsorption. The in vitro cell culture test was conducted on the scaffolds with human mesenchymal stem cells (hMSCs). The cells on PLLA/n-HA/ds-DNA scaffold showed more significant increases than neat PLLA and PLLA/n-HA scaffolds.

© 2014 Elsevier Ltd. All rights reserved.

## 1. Introduction

Tissue engineering applies methods from materials engineering and life science to create artificial constructs for regeneration of new tissue [1,2]. With tissue engineering we can create biological substitutes to repair or replace the failing organs or tissues. One of the most promising approaches towards this direction is to grow cells on scaffolds-highly engineered structures that act as temporary support for cells which facilitate the regeneration of the target tissues without losing the three dimensional (3D) stable structure.

Polymeric scaffolds play a pivotal role in tissue engineering through cell seeding, proliferation, and new tissue formation in three dimensions, showing great promise in the research of engineering a variety of tissues. Pore size, porosity, and surface area are widely recognized as important parameters for tissue engineering scaffold. Other architectural features such as pore shape, pore wall morphology, and interconnectivity between pores of the scaffolding materials are also suggested to be important for cell seeding, migration, growth, mass transport and tissue formation [1].

Bioactive ceramics such as hydroxyapatite (HA) and calcium phosphates (CPs) are another major class of biomaterials for bone repair [3,4]. They showed appropriate osteoconductivity, (only certain types are osteoinduction, i.e., new bone formation [5]) and biocompatibility because of their chemical and structural similarity to the mineral phase to native bone. However, the disadvantage is their inherent brittleness and poor shape ability. For this reason, polymer/bioactive ceramic composite scaffolds have been developed in application for the bone tissue engineering [6]. They exhibit good bioactivity, manipulation and control microstructure in shaping to fit bone defects [7].

Apart from this, adsorption of DNA on HA has been extensively investigated [8,9]. HA particles have various ions on their surfaces (e.g., $Ca^{2+}$, $CaOH^+$, $PO_4^{3-}$, $HPO_4^{2-}$, $H_2PO_4^-$, and $CaH_2PO_4^+$). The positive surface charge is attributed to the increasing adsorption of $H^+$ or the loss of $OH^-$ [10]. The interaction is generated between negatively charged phosphate ($PO_2^-$) groups along the backbone of the DNA and $Ca^{2+}$, $CaOH^+$ and $CaH_2PO_4^+$.

* Corresponding author. Tel.: +81 (0)528091861; fax: +81 (0)528091864.
E-mail address: okamoto@toyota-ti.ac.jp (M. Okamoto).

HA nanoparticles are suitable as drug-delivery system, especially for high transfection of cells with DNAs [9,11]. The introduction of DNA, RNA, or oligonucleotides into eukaryotic cells is called transfection. This process involves the uptake of extracellular molecules trough the cell membrane into the cytoplasm and also into the nucleus. When DNA is brought into the nucleus, it can be incorporated into a cell's genetic material and induce the production of specific proteins [12].

Scaffold mediated gene delivery is an advantageous strategy for gene transfer. It enables localized delivery of a therapeutic gene. The surrounding cells at the implant site principally take up the DNA delivered from the scaffold, therefore limiting unwanted exposure in other areas [13]. The scaffold structure allows for sustained gene delivery acting as a reservoir, which gradually releases DNA/CP complex over time. The degradation rate of the scaffold material can be designed so that the required release rate is achieved [14]. Another advantage of the scaffold is its role in the protection of the DNA/CP complex.

Current trends in tissue engineering seek the scaffold with gene delivery complex, as well as stimulatory functions promoting cell proliferation and new tissue formation in 3Ds [15].

The aim of this study is examine the adsorption of double-stranded DNA (ds-DNA) having small base pairs (bps) on 3D scaffolds with incorporation of HA particles. We conducted the fabrication of highly porous and interconnected biodegradable polymer scaffolds based on the poly-L-lactide (PLLA) with HA particles produced using a thermally-induced phase separation (TIPS) method [16].

The microarchitectural properties of the PLLA/HA composite scaffolds, in particular its morphology and porosity were analyzed. The propensity and morphology of the composite scaffolds to adsorb the ds-DNA molecules was studied and correlated with the results of the in vitro cell culture analyzed the cell−scaffold interaction using the colonization of human mesenchymal stem cells (hMSCs).

## 2. Experimental section

### 2.1. Materials

A commercial PLLA with a D content of 1.1−1.7% ($M_w = 150$ kDa, $M_w/M_n = 1.56$, $T_g \sim 60$ °C, $T_m \sim 169$ °C) supplied by Unitika Co. Ltd., Japan was dried under vacuum at room temperature. A natural HA (n-HA) from calf bones was purchased from Eccera Ltd., Japan (particle diameter of ~1 μm, Ca/P molar ratio of 1.64).

In this study, ds-DNA from salmon sperm (Sigma−Aldrich: D31149) was used. The weight-average molecular weight ($M_w$) was 4.6 kDa possessing 7 bps (see Section 3.4) together with a high aspect ratio (approximate strand length of ~2.4 nm [17] and diameter of ~2 nm [18]). 1,4-dioxane as a solvent, HCl and NaOH were purchased from Nacalai Tesque, Kyoto. Millipore Milli Q ultrapure (specific resistance: 18 MΩ cm, total organic carbon (TOC) < 20 ppb, Merck Millipore Japan Co.) water through dialysis membrane was used in all experiment.

### 2.2. Preparation of PLLA/n-HA composite scaffolds

The mixture of PLLA pellet and n-HA crystal powder (PLLA/n-HA = 50/50 wt.%) was dispersed in a solvent (1,4-dioxane) with different concentration by sonication at 100 W (Ultrasonic 250, Hey Co.) usually for 30 min to obtain a suspension. The suspensions were maintained in a freezer at −20 °C overnight to solidify and induce solid−liquid phase separation. The solidified mixtures were transferred into freeze-dryer vessel (FDU-2200, Eyela Ltd.) under 10 Pa at −80 °C for 3 h to remove solvent. The prepared samples

were designated as *p*-PLLA/n-HA-*x* (*x*: polymer solution concentration of 1.0, 1.67, 2.5, and 5.0 wt.%) and '*p*-' refers to the porous scaffold. For a comparison, *p*-PLLA-5.0 without n-HA was prepared via same procedure.

### 2.3. Characterization

The pore morphology was observed through field emission scanning electron microscope (FE-SEM: SU6600, Hitachi Ltd.) equipped with elemental analysis by energy dispersive X-ray spectrometry (EDX: INCA *x*-act, Oxford instruments). The operated accelerating voltage was 15 kV and the specimens were coated with a thin layer of gold and palladium (Au/Pd 6:4) with a thickness of ~20 nm.

The function for determining pore density ($N_p$) in cm$^{-3}$ is defined as the following Equation (1) [19]

$$N_p = \left[\frac{n}{A}\right]^{3/2} \left[\frac{\rho_b}{\rho_{sc}}\right] \tag{1}$$

where $n$ is the number of pores in the area ($A$) of micrograph. The mass density of both bulk ($\rho_b$) and scaffolds ($\rho_{sc}$) in g/cm$^3$ samples were estimated by using the buoyancy method [19].

The porosity ($\Phi_p$) can be measured using the following equation [20]:

$$\Phi_p = \left[1 - \frac{\rho_{sc}}{\rho_b}\right] \tag{2}$$

The surface charge characteristic of the ds-DNA molecules in water (0.1 wt.%) was determined by electrophoresis at 25 °C (Zetasizer Nano ZS, Malvern Instruments, UK) by the technique of laser Doppler anemometry. The method involved adjusting the pH of suspension in the range of 3−11 by using dilute HCl and NaOH. All measurements were performed for five replicates and averaged to get the final value. n-HA in water (0.1 wt.%) was also measured to understand the surface charge characteristic of the particles on the composite scaffolds.

Dynamic light scattering (DLS) was also conducted to measure the size and distribution of the ds-DNA molecules in water (0.1 wt.%) by using Zetasizer Nano ZS (wavelength = 532 nm). The dynamic information can be retrieved by examining the autocorrelation function $g(t)$ of the time-dependent intensity. A time correlation function $G(t)$ can be defined, which is related to $g(t)$ by Ref. [21]

$$g(t) = B\left[1 + G^2(t)\right] \tag{3}$$

where $B$ is a base line term.

Using cumulant method (ISO 13321) [21], we employed single exponential function in $G(q, t)$.

$$G(t) = \exp\left(-D_T q^2 t\right) \tag{4}$$

$D_T$ is the translational diffusion coefficient of molecules, which corresponds to the rate of correlation decay, and $q$ is the scattering vector. The Equation (4) reduced by the Einstein−Stokes law:

$$R_H = k_b T / 6\pi\eta_s D_T \tag{5}$$

where $R_H$ is the hydrodynamic radius, $k_b$ is the Boltzmann constant, and $\eta_s$ is the viscosity of the water.

Electrophoresis was performed using microchip electrophoresis system (MultiNA, Shimadzu Co.) in 10 mM Tris−HCl buffer solution without polymerase chain reaction. The samples prepared from ds-

DNA and the supernatant solution after adsorption of ds-DNA were 0.5—1.0 ng/μL with the addition of 50 mM KCl and 1.5 mM MgCl₂. The DNA ladder indicators for a standard range from 10 to 500 bps were used to judge the electropherograms [22].

The thermal properties were analyzed using the temperature-modulated differential scanning calorimetry (TMDSC) (TA 2920, TA Instruments) at a heating rate of 5 °C/min with a heating/cooling cycle of the modulation period of 60 s and an amplitude of ±0.769 °C, to determine heat of fusion, the DSC was calibrated with Indium before experiments.

For the measurement of degree of crystallinity ($\chi_c$) prior to TMDSC analysis, the extra heat absorbed by the crystallites formed during heating had to be subtracted from the total endothermic heat flow due to the melting of the whole crystallites. This can be done according to the principles and procedures described in our previous paper [23]. In the TMDSC experiments, the endothermic heat flow $\Delta H_{different}$ of the initially existing crystallites can be easily calculated as $\Delta H_{difference} = \Delta H_{rev} - \Delta H_{nonrev}$, where $\Delta H_{rev}$ is the endothermic melting (reversing) enthalpy from the reversing heat flow profile and $\Delta H_{nonrev}$ is the exothermic ordering/crystallization (nonreversing) enthalpy from the nonreversing heat flow profile appearing in the temperature range of −30—200 °C. The $\chi_c$ was thus calculated as $\Delta H_{difference}/\Delta H^o$ with $\Delta H^0 = 93$ J/g, which is the melting enthalpy of 100% crystalline PLLA [24].

Fourier transform infrared (FTIR) spectroscopic imaging measurements were preformed using a Perkin—Elmer Spectrum Spotlight 400 Microscope System. This system is equipped with a liquid N₂ cooled Mercury—Cadmium—Telluride MCT detector. To construct FTIR maps, spectra were collected in continuous scan mode for sample area of 200 × 200 μm² with a resolution of 1.65μm/pixel by one scan for each spectrum of the fabricated scaffolds under the Ge attenuated total reflectance (ATR) crystal. Spectra were collected in the spectral range 4000—680 cm⁻¹ with a resolution of 8 cm⁻¹ and integrated by taking the areas under the curve between the limits of the peaks of interest. Data acquisition was carried out by means of the Spotlight software package.

### 2.4. Adsorption experiments

*p*-PLLA/n-HA-5 was dispersed in aqueous adsorbate solutions. As a reference, n-HA particles were used as adsorbent. 10 mg of *p*-PLLA/n-HA-5 and/or n-HA particles with 10 mL of 1.11—143.0 μM aqueous solutions for ds-DNA were mixed. In addition, 5—10 μL of dilute HCl solution was added in each solution and adjusted to the pH 4.0. Millipore Milli Q ultrapure water (18 MΩ cm, total organic carbon (TOC) < 20 ppb) through dialysis membrane was used without Tris—HCl buffer solution for all experiments [25].

The mixtures were shaken well for 60 h at 25 °C. 60 h was fixed as the equilibrium time throughout this study because adsorption uptake approached the constant value. After equilibrating ds-DNA adsorption, the supernatant solutions were collected after centrifuge at a speed of 5000 rpm for 20 min. The total organic carbon (TOC) and total nitrogen (TN) of supernatant solutions were measured by using combustion method with a set temperature of 800 °C after four point calibration using an instrument (multiN/C 2100S, Analytik Jena) [22].

The amount of adsorption ($Q_{ads}$) increases with the equilibrium concentration of adsorbate ($[A]_e$). The adsorption isotherms were fitted by the Freundlich equation [26] ($r^2 \geq 0.92$).

$$Q_{ads} = K_f\,[A]_e^{1/N} \qquad (6)$$

where $K_f$ is the relative adsorption capacity of the adsorbent and $N$ is the adsorption intensity, which describes the shape of the isotherm. For FTIR spectroscopic imaging, the ds-DNA solution before adsorption was 90.0 μM.

### 2.5. In vitro cell culture

Human mesenchymal stem cells (hMSCs) were used for in vitro cell culture to analyze the biocompatibility of the materials. The cells were maintained in mesenchymal stem cell growth medium (MSCGM), which consisted of low-glucose Dulbecco's modified essential medium (DMEM) (Life Technologies) supplemented with 10% heat-inactivated fetal bovine serum (FBS, WiCell), 100 unit/mL penicillin (Invitrogen), and 100 μg/mL streptomycin (Invitrogen). The medium was changed daily and non-adherent cells were removed by medium replacement.

Prior to culture initiation, the composite scaffolds were cut into small pieces of roughly 5 × 20 × 2 mm³ and sterilized with ethanol at room temperature. To further ensure sterilization, samples were subsequently exposed to germicidal UV light for 2 h on each side, and then placed into 6-well tissue culture-treated polystyrene plates. Next, 2 mL of the MSCGM medium containing hMSCs was seeded onto the surface of the sterilized composite scaffolds at a density of 6 × 10⁵ cells/cm². The seeded samples were incubated at 37 °C for an hour to provide the cells a chance to adhere onto the surface of the scaffolds. Additional media was then added to each well to allow long-term culture of the seeded scaffolds. The cultures were incubated in an atmosphere of 5% CO₂ at 37 °C for a period of seven days. The cell culture media was changed daily with the cell activity checked on the 3rd and 7th days after seeding.

### 2.6. Cell viability

The survivability of the seeded cells was quantified using a Live/Dead Cytotoxicity Kit (Invitrogen) according to manufacturer's instructions. This kit utilizes Calcein-AM and EthD-1 to label living and dead cells, respectively. Calcein-AM is a cell-permeable dye that gets converted into a strong green light-emitting compound after contact with intracellular esterases that are present in living cells. EthD-1 is a DNA-intercalating agent that can only penetrate damaged cell membranes of dead cells, upon which it emits orange/red fluorescence when inserted into the DNA double helix. After staining, the labeled cells were viewed under a fluorescence confocal microscope (Nikon A1RsiTi-E, Nikon).

To quantify cell viability, at least 7 square fields were randomly surveyed and the number of alive (green) and dead (red) cells was counted. Relative cell viability values were then calculated as the
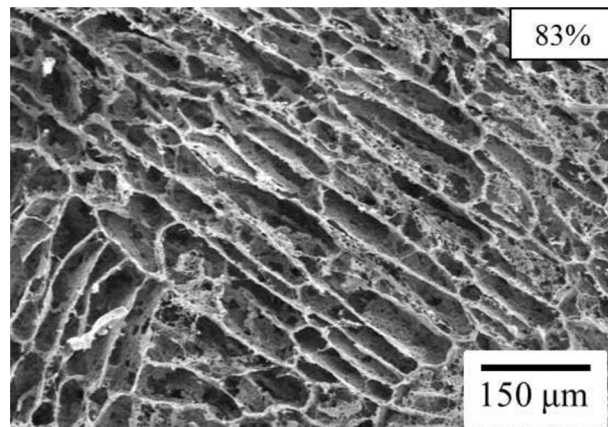


**Fig. 1.** FE-SEM image of *p*-PLLA-5 scaffold. The number in the box shows the porosity.

averaged area of live cells per unit area on each substrate. The area of live cells was analyzed by ImageJ software.

### 2.7. Statistics

All data presented are expressed as the mean and standard deviations ($\pm$SD). Statistical analysis was performed using the Student's $t$-test to compare the difference between experimental groups. $p < 0.05$ was considered statistically significant.

## 3. Results and discussion

### 3.1. PLLA/HA composite scaffolds

The concentration of the solution is one of the factors that determine the porosity ($\Phi_p$) because the solvent crystals became pores after subsequent sublimation via TIPS. Therefore, a porous structure having $\Phi_p \sim 0.85$ could be prepared. Fig. 1 shows FE-SEM image of pore morphology of neat PLLA porous structure (p-PLLA-5) fabricated by the solution concentration of 5 wt.%. The pore sizes of p-PLLA-5 are in the range of 25—160 $\mu$m. The pores exhibit closed structure having an anisotropy feature due to the temperature gradient along the solvent crystallization direction [1]. After a close look, on the pore walls, the pore size in this area shows much smaller (~6 $\mu$m) with a regular structure. The calculated value of $\Phi_p$

is 0.83. This result suggests that an increase in pore connectivity leads to much higher $\Phi_p$ value of the scaffold.

Fig. 2 shows FE-SEM images of the fabricated p-PLLA/n-HA scaffolds with different concentrations of dioxane. For p-PLLA/n-HA-5 fabricated by the solution concentration of 5.0 wt.%, shows the isotropy closed pore structure having small pore size accompanied with more narrow pore distribution and the large number of $N_p$ as compared with that of p-PLLA-5. The incorporation of n-HA in dioxane solution has a significant contribution to retard the growth and coalescence of crystallized dioxane phases under TIPS. The n-HA particles in the polymer solution perturbed the solvent crystallization to some extent and thereby made the pore structure more isotropic. The low concentration of n-HA leads to the high porosity, i.e., up to 87% (for p-PLLA/n-HA-1), which is considered to be beneficial for pore ingrowth and survival. The solvent concentration has much effect on the porosity and pore morphology. The morphological parameters of the scaffolds are presented in Table 1.

The degree of the crystallization of PLLA in the pore wall is around 45%. The HA particles might not act as nucleating sites for PLLA crystallization. For p-PLLA/n-HA-1.67 and p-PLLA/n-HA-1, the pore wall surfaces is not smooth, and appear as loose fibrous structure with several microns in between. The n-HA particles are entrapped in the fibrous structure in the open pore scaffolds in the enlarged view (Fig. 2(e) and (f)). These results suggest that the
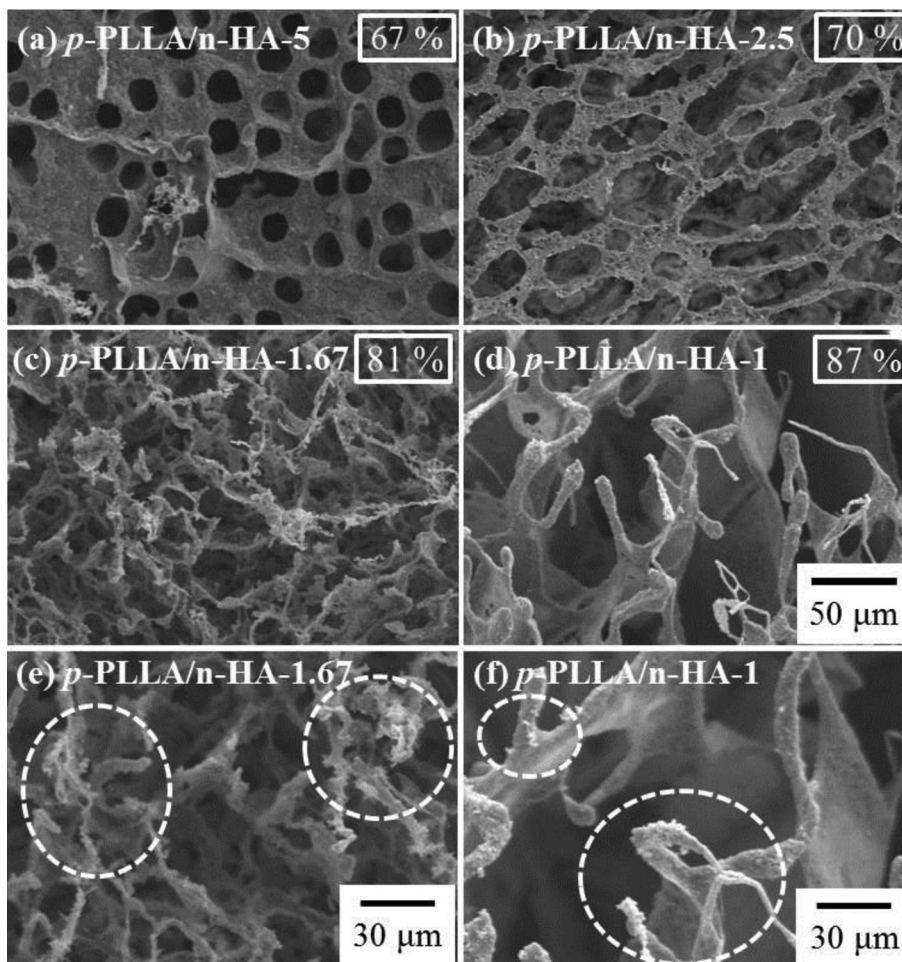


**Fig. 2.** FE-SEM images of p-PLLA/HA scaffolds: (a) p-PLLA/n-HA-5, (b) p-PLLA/n-HA-2.5, (c, e) p-PLLA/n-HA-1.67, and (d, f) p-PLLA/n-HA-1. The circled areas indicate the n-HA particles are entrapped in the fibrous structure in the open pore scaffolds (see text). The number in the box shows the porosity.

**Table 1**
Morphological parameters and degree of crystallinity of scaffolds.

| Samples | Polymer conc./wt.% | Pore structural factor | | | $\Phi_p$/% | $\chi_c$/% |
|---|---|---|---|---|---|---|
| | | 2 $d$/µm | $N_p$/cm$^{-3}$ | $\delta^a$/µm | | |
| p-PLLA-5 | 5.0 | 25–160 | $5.30 \times 10^5$ | 6.9 | 83 | 47.2 |
| p-PLLA/n-HA-5 | 5.0 | 14–36 | $1.30 \times 10^7$ | 12.7 | 67 | 45.0 |
| p-PLLA/n-HA-2.5 | 2.5 | 15–115 | $6.38 \times 10^6$ | 11.9 | 70 | 48.5 |
| p-PLLA/n-HA-1.67 | 1.67 | o.p.[b] | – | 4.3 | 81 | 50.2 |
| p-PLLA/n-HA-1 | 1.0 | o.p.[b] | – | 3.0 | 87 | 52.6 |

[a] Mean pore wall thickness determined from the data of FE-SEM observation.
[b] Open pore structure.

newly developed PLLA/n-HA-based composite scaffolds may be a superior material for bone tissue engineering.

### 3.2. Surface charge characteristics

The phosphate groups of ds-DNA molecules possess a negative charge ($PO_2^-$). The zeta potential values for the surface of the ds-DNA are negative over the entire pH range from 3 to 11 and even more smaller negative (~−45 mV) at a lower pH value, which may be attributed by the acquiring protons to the phosphate groups on the acid side (Fig. 3). Furthermore, the values decrease with continuous increase to attain −55 mV at pH 5.5. Beyond pH 5.5, the zeta potential values increase again, presumably due to the two differently charged two substituted purine groups [27].

The results of the zeta potential measurements of n-HA are shown in Fig. 3. The isoelectric point ($I_p$) of n-HA has the pH range from 5 to 8, where the zeta potential values remain constant ~ −0.2 to −0.8 mV [28]. In the pH range 5–8, both positively and negatively charged species are present on the surface of the n-HA particles [11]. On dispersion into water, the n-HA particles have various ions on their surfaces (e.g., $Ca^{2+}$, $CaOH^+$, $PO_4^{3-}$, $HPO_4^{2-}$, $H_2PO_4^-$, and $CaH_2PO_4^+$), as mentioned before. The positive surface charge is attributed to the increasing adsorption of $H^+$ or the loss of $OH^-$ [10], and vice versa in case of the negative surface charge. The highest (+7.6 mV at pH 3.05) and lowest (−8.8 mV a pH 10.86) values are found for n-HA. In both pH regions the n-HA particles are stabilized electrostatically due to the high surface charge [29]. The main reason for the adsorption is due to the interaction between negatively charged phosphate ($PO_2^-$) groups along the backbone of the ds-DNA and positive surface charges ($Ca^{2+}$ and $CaOH^+$) of the n-HA particles.
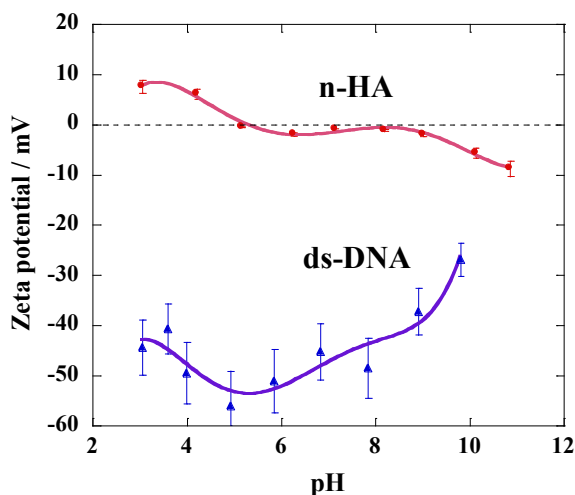


**Fig. 3.** Zeta potential versus pH of ds-DNA and n-HA. Results are expressed as mean ± S.D. ($n = 5$).
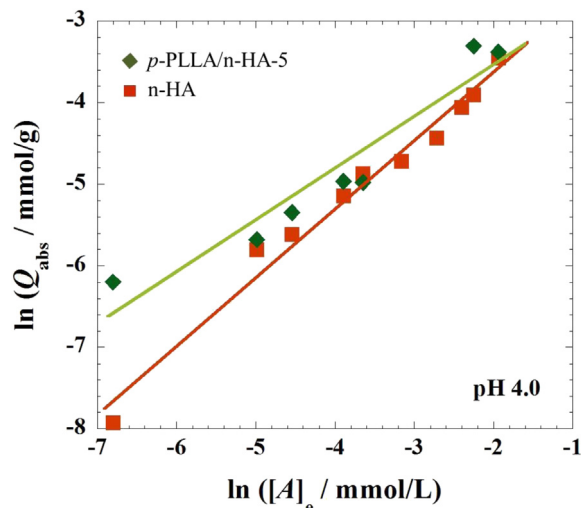


**Fig. 4.** Plots of ln ($Q_{ads}$) versus ln ($[A]_e$) for p-PLLA/n-HA-5 and n-HA at pH 4.0.

### 3.3. Adsorption capacity of ds-DNA

The adsorption features of ds-DNA on the scaffold (p-PLLA/n-HA-5) at pH 4.0 were examined to clarify the interaction generated between the phosphate groups and the n-HA particles entrapped on the scaffold surfaces (Fig. 4). The isotherms were fitted the by Freundlich equation with $r^2$ values $\geq 0.92$, and the values are listed in Table 2. Because Freundlich isotherms typically describe systems where saturation is not observed, like in this experiment. The adsorption capacity of ss-DNA by p-PLLA/n-HA-5 exhibits same order of magnitude as compared with that of n-HA particles. The ds-DNA molecules can more easily adsorb on the large surface area of the scaffold from lower (1.11 µM) up to higher concentration (0.143 mM) of ds-DNA. The adsorption isotherms exhibited a marked curvature, with slopes (1/$N$) significantly < 1.0, indicating a convex up curvature, or $L$-type isotherm. The slope of the isotherms steadily decreased with increasing adsorptive concentration because the vacant sites became less accessible with the progressive covering of the adsorbent surface [30].

### 3.4. Electrophoresis analysis

Using electrophoresis analysis we observed that the structure of ds-DNA is changed upon adsorption on p-PLLA/n-HA-5 surfaces. Before adsorption of the pristine ds-DNA, the appearance of main peak is observed at 7 bps having size range from 1 to 50 bps, whereas the remnant shoulder is located around 14–18 bps size (indicated the arrow) (Fig. 5(a)). As conjectured, the distribution is broad owing to the heterogeneous base composition of the salmon sperm DNA. For the supernatant solution of ~9% adsorption of ds-DNA (feed $[A]_e = 90.0$ µM) on the p-PLLA/n-HA-5 surfaces, the elution profile in the electropherogram remains the short bps around the DNA ladder indicators for a standard range from 1 to 26 bps (Fig. 5(b)). The electropherogram for ~19% adsorption of ds-DNA (feed $[A]_e = 90.0$ µM) on the n-HA-5 particles exhibits the

**Table 2**
Adsorption parameters of ds-DNA on p-PLLA/n-HA-5 and n-HA.

| Samples | $K_f$/mmol/g mmol/l$^{-1/N}$ | $N$ - | $r^{2a}$ |
|---|---|---|---|
| p-PLLA/n-HA-5 | $1.02 \times 10^{-1}$ | 1.57 | 0.92 |
| n-HA | $1.44 \times 10^{-1}$ | 1.19 | 0.98 |

[a] The values are calculated by a log–log linear regression.
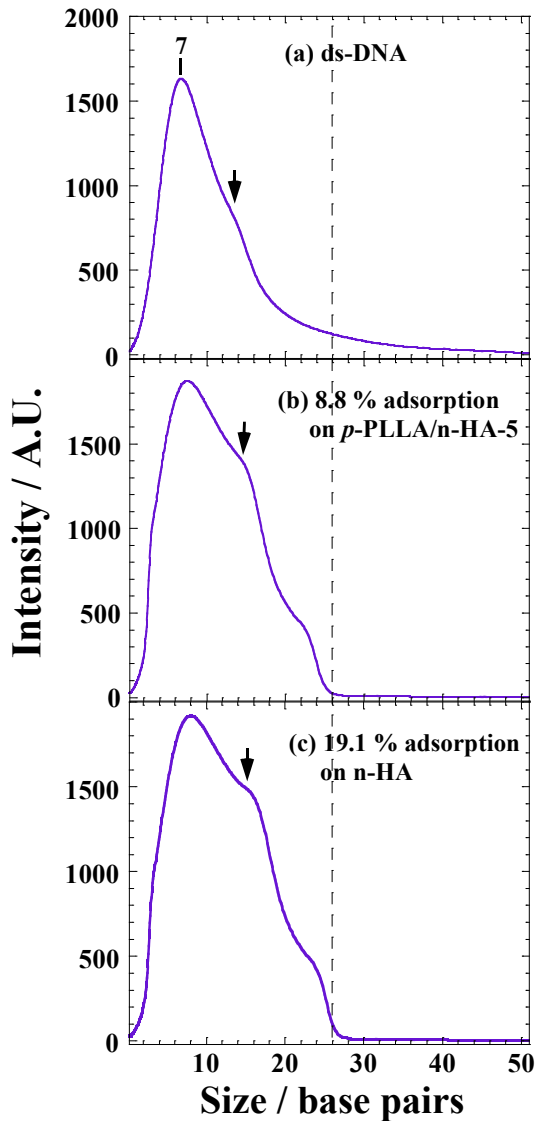
**Fig. 5.** Electropherograms: (a) pristine ds-DNA (salmon sperm); (b) supernatant solution of 8.8% adsorption of ds-DNA on *p*-PLLA/n-HA-5 surfaces; (c) supernatant solution of 19.1% adsorption of ds-DNA on n-HA-5 particles. The arrows indicate the small remnant shoulders. The dashed line indicates the position of the 26 bps (see text).

profile similar to that of ~9% adsorption (Fig. 5(c)). The peak mainly consists of long molecule for a standard range above 26 bps where it disappears (marked with the dashed line). The reason is not obvious at present. However, what is striking in our observation is the magnitude of the mobility of DNA molecules on the surfaces of *p*-PLLA/n-HA-5 and/or n-HA particles for the desorption process. Thus, we need to consider the possibility that the short bps in DNA cause desorption of the DNA molecules from the surfaces.

### 3.5. DLS measurement and FTIR spectroscopic imaging

At low pH (= 4.0), the average particle size of ds-DNA is around 200 nm with polydispersity index of 0.24 as revealed by DLS study (Fig. 6). The DLS data also shows that the distribution is clearly asymmetric. Since the ds-DNA used in this work has size ranged from 1 to 50 bps, and a fully stretched length up to 17 nm, this suggests that the aggregate of the ds-DNA molecules is observed.
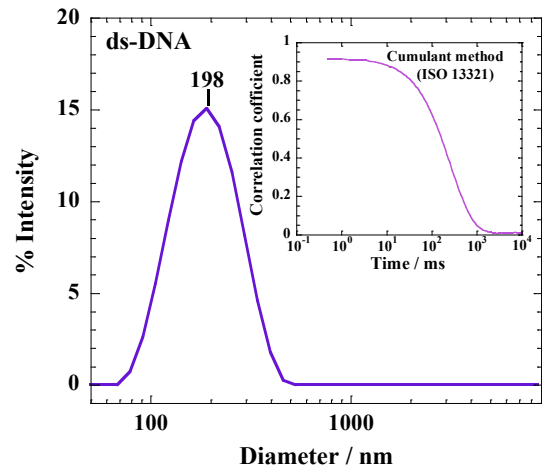


**Fig. 6.** DLS particle size distribution of ds-DNA in water (0.1 wt.%), performed at pH 4.0. The inset is a normalized correlation function (time variation of the correlation coefficient).

Fig. 7 shows typical spectra of the fabricated scaffolds in the region of 2000−680 cm$^{-1}$. For *p*-PLLA-5 (Fig. 7(a)), the carbonyl stretching $\nu$(C=O) absorption band of PLLA at 1754 cm$^{-1}$ is observed. A peak observed at 1211 cm$^{-1}$ is assigned to the coupled C−O stretching vibrations aligned in a direction perpendicular to the helix axis of PLLA, while another peak at 1186 cm$^{-1}$ is
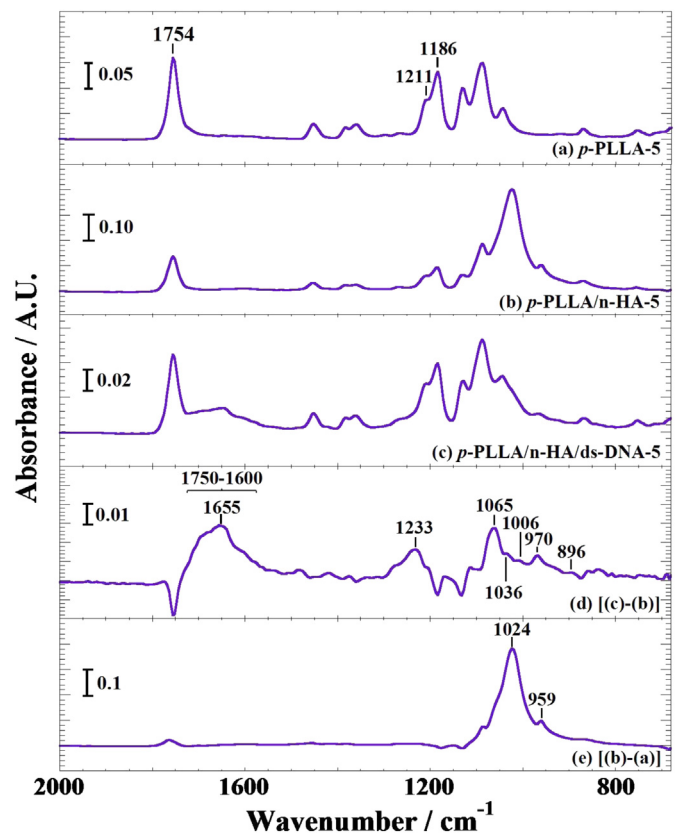


**Fig. 7.** FTIR spectra obtained from the selected 200 × 200 μm$^2$ scaffold areas: (a) *p*-PLLA-5, (b) *p*-PLLA/n-HA-5, and (c) *p*-PLLA/n-HA-5/ds-DNA in the region of 2000−680 cm$^{-1}$. Difference spectra of (d): [(c)−(b)] to obtain the spectrum of the adsorbed ds-DNA molecules, and (e): [(b)−(a)] to obtain the spectrum of the entrapped n-HA particles.
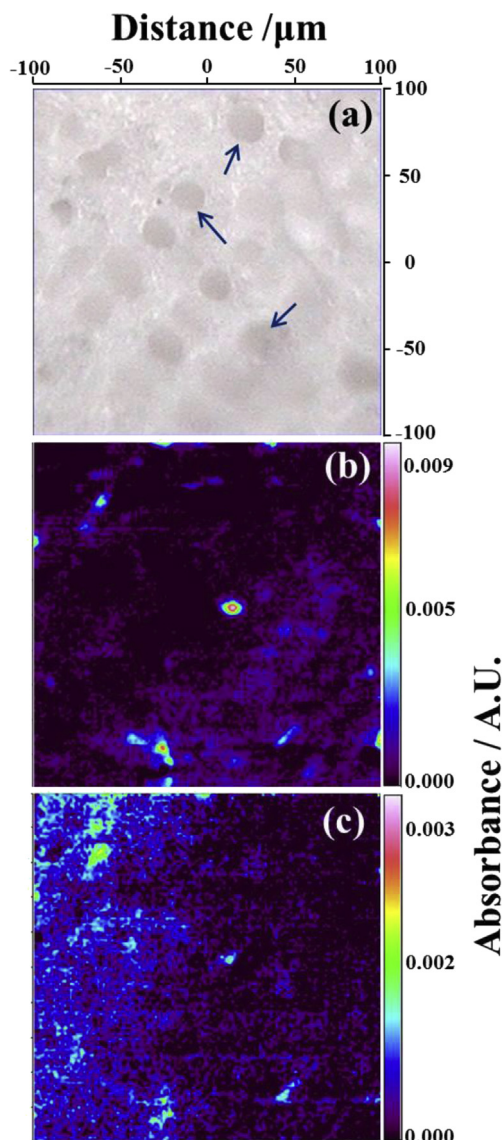
**Fig. 8.** FTIR images obtained from the selected 200 × 200 μm² p-PLLA/n-HA-5/ds-DNA scaffold areas: (a) visible image (the dark areas correspond to the pore and bright area is crystallized PLLA matrix, as marked with the arrows), (b) distribution of the adsorbed ds-DNA molecules based on the absorption band at 1665 cm⁻¹, and (c) distribution of the entrapped n-HA particles based on the absorption band at 959 cm⁻¹. The red area indicates a region of high concentration while blue area indicates a low concentration in color-coded images. (For interpretation of the references to colour in this figure legend, the reader is referred to the web version of this article.)

assignable to the vibrations aligned parallel to the helix axis of PLLA [31]. By subtracting the each spectrum, i.e., p-PLLA-5, p-PLLA/n-HA-5 (Fig. 7(b)), and p-PLLA/n-HA-5/ds-DNA (Fig. 7(c)) from the consecutive spectra, a difference spectrum can be achieved. Fig. 7(d) shows the difference spectra between p-PLLA/n-HA-5/ds-DNA and p-PLLA/n-HA-5, which corresponds to the ds-DNA. The bands located in the region of 1750–1600 cm⁻¹, which are common to C=O, C=N, C=C stretching and exocyclic −NH₂ bending vibrations in the DNA bases [32]. The sensitive bands at 1233 cm⁻¹ (asymmetric stretching mode of PO₂⁻ groups: $\nu_{as}(PO2^-)$), and 1065 cm⁻¹ (stretching of ribose $\nu$(C−C)) of the phosphodiester-deoxyribose backbone provide valuable information. The B-form DNA shows characteristic absorbance peaks at 1036 (double-stranded DNA in B-form), 970 and 896 cm⁻¹ as seen in the region from 1065 to 850 cm⁻¹.

In Fig. 7(e) shows the spectrum of the entrapped n-HA particles. The calcified zones shows some strong convoluted band at ~ 1024 cm⁻¹. However, this band could not be used due to overlap with a characteristic peak of the B-form. FTIR images are generated by plotting the variation of the absorption band at 1665 cm⁻¹ and the band at 959 cm⁻¹ to illustrate the relative distribution of the adsorbed ds-DNA and the entrapped and dispersed n-HA on the PLLA scaffolds, respectively, as shown in Fig. 8.
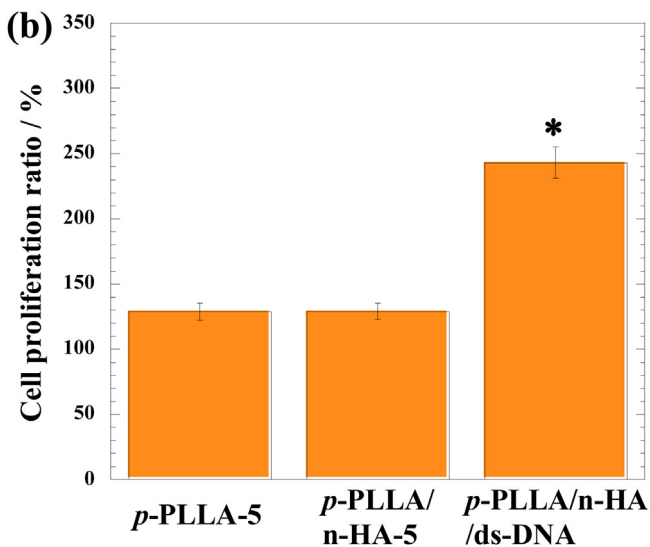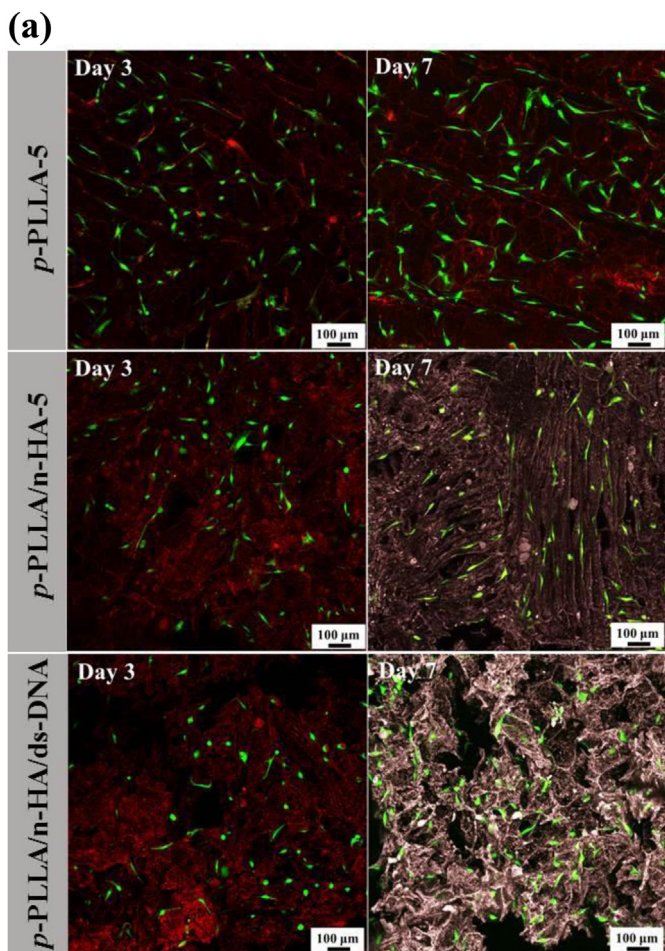
Fig. 8(b) and (c) show the distribution of the adsorbed ds-DNA and entrapped n-HA on the PLLA. The shape of the adsorbed ds-DNA domains is well defined with a size of ca. 3–6 μm. The domains are larger than the aggregated ds-DNA molecules before adsorption, which was estimated by DLS (~200 nm). This is due to some extent of agglomeration during adsorption process on the scaffold surfaces. The adsorbed ds-DNA in mass per unit mass of p-PLLA/n-HA-5 is 36.0 mg/g (= 3.6 wt.%). This adsorbed amount of ds-DNA is consistent with the distribution image (Fig. 8(b)).

In Fig. 8(c), no sharp interface between different domains can be observed because the absorption band used to generate this image was not significantly strong compared to that of ds-DNA. As expected the interaction between negatively charged phosphate (PO₂⁻) groups along the backbone of the ds-DNA and positive surface charges (Ca²⁺ and CaOH⁺) of the entrapped n-HA particles, the positions of the ds-DNA coincide with the spectral manifestation of the n-HA. It should be noted that the ds-DNA molecules are adsorbed by the entrapped n-HA particles as revealed by FTIR spectroscopic imaging approach.

### 3.6. Cell growth

Day 3 fluorescent images of hMSCs indicated that cells successfully attached onto the surfaces of the composite scaffolds (Fig. 9(a)). The n-HA is bioactive ceramics for bone repair and shows appropriate osteoconductivity and biocompatibility because of their chemical and structural similarity to the mineral phase to native bone [3,4]. As compared with neat PLLA scaffold (p-PLLA-5), slightly less live cells are detected on the composite scaffold (p-PLLA/n-HA-5) and ds-DNA modified scaffold (p-PLLA/n-HA-5/ds-DNA), which indicated that the addition of n-HA particles may have not been beneficial for cell attachment and proliferation on the scaffold in this study. However, after 10 days of cell culture, the levels of EthD-1 in the images show that the modification by ds-DNA has obvious effect on the cell growth. The cell count statistical results shown in Fig. 9(b) indicate significant cell proliferation from day 3 to day 7, and significantly more cells on p-PLLA/n-HA-5/ds-DNA than on p-PLLA-5 and p-PLLA/n-HA at the day 10 point. Therefore these results suggest the scaffold surface modification by sd-DNA has favorable biocompatibility with hMSCs.

The cytotoxicity depends on the charge on the surface of the molecules. Negatively charged molecules shows lower unfavorable effect on the cells viability [33]. Because the cell membrane consisting of phospholipid bilayers with negative charge (~−20 mV) play an important roll to separate the cytoplasm from the outside environment and modulate the movement of the molecules in and out of the cell [34]. The positively charged molecules are more effectively adsorbed on the cell membrane as compared with the negatively charged or neutral ones. However, the positively charged molecules cause the plasma membrane disruptions as reported by several researchers [35–37]. The plasma membrane disruptions are probably a common property of the cationic molecules [38]. In this regard, the negatively charge ds-DNA molecules on the scaffold (p-PLLA/n-HA-5/ds-DNA) did not exhibit any observable toxic effect in this study. The real mechanism for this requires further investigation.

**(a)**

the growth and coalescence of crystallized dioxane phases under TIPS. The n-HA particles in the polymer solution perturbed the solvent crystallization to some extent and thereby made the pore structure more isotropic. The adsorption features of ds-DNA on the scaffold (p-PLLA/n-HA-5) at pH 4.0 were examined to clarify the interaction generated between the phosphate groups and the n-HA particles entrapped on the scaffold surfaces. The ds-DNA molecules can more easily adsorb on the large surface area of the scaffold from lower (1.11 μM) up to higher concentration (0.143 mM) of ds-DNA. FTIR spectroscopic imaging approach demonstrated the shape of the adsorbed ds-DNA domains on the scaffold surfaces was well defined with a size of ca. 3—6 μm. The in vitro cell culture test was conducted on PLLA/n-HA-5/ds-DNA scaffolds with hMSCs. The cells on p-PLLA/n-HA-5/ds-DNA scaffolds showed more significant increases than neat PLLA and p-PLLA/n-HA-5 scaffolds. These results suggested that the newly developed PLLA/n-HA-5 modified by ds-DNA might be a superior material for tissue engineering.

## Author contributions

The manuscript was written through contributions of all authors. All authors have given approval to the final version of the manuscripts.

## Notes

The authors declare no competing financial interest.

## References

[1] Ma PX. Scaffolds for tissue fabrication. Mater Today 2004;7:30—40.
[2] Langer R, Vacanti JP. Tissue engineering. Science 1993;260:920—6.
[3] Hench LL. Bioceramics. J Am Ceram Soc 1998;81:1705—28.
[4] Kim HW, Knowles JC, Kim HE. Hydroxyapatite/poly(epsilon)-caprolactone) composite coating on hydroxyapatite porous bone scaffold for drug delivery. Biomaterials 2004;25:1279—87.
[5] LeGeros RZ. Calcium phosphate-based osteoinductive materials. Chem Rev 2008;108:4742—53.
[6] Ghosh SK, Nandi SK, Kundu B, Datta S, De DK, Roy SK, et al. In vivo response of porous hydroxyapatite and beta-tricalcium phosphate prepared by aqueous solution combustion method and comparison with bioglass scaffolds. Acta Biomater 2013;86:217—27.
[7] Zhang R, Ma PX. Porous poly(l-lactic acid)/apatite composites created by biomimetic process. J Biomed Mater Res 1999;45:285—93.
[8] Pakroppa W, Müller W. Fractionation of DNA on hydroxyapatite with a base-specific complexing agent. Proc Natl Acad Sci 1974;71:699—703.
[9] Chen W, Lin M, Lin P, Tai P, Chang Y, Yamamoto S. Studies of interaction mechanism between single strand and double-strand DNA with hydroxyapatite by microcalorimetry and isotherm measurement. Colloids Surf A 2007;295:274—83.
[10] Skartsila K, Spanos N. Surface characterization of hydroxyapatite: potentiometric titrations coupled with solubility measurements. J Colloid Interface Sci 2007;308:405—12.
[11] Sokolova V, Epple M. Inorganic nanoparticles as carriers of nucleic acids into cells. Angew Chem Int Ed 2008;47:1382—95.
[12] McNeil SE, Perrie Y. Gene delivery using cationic liposomesa. Expert Opin Ther Pat 2006;16:1371—82.
[13] Jang J-H, Rives CB, Shea LD. Plasmid delivery in vivo from porous tissue-engineering scaffolds: transgene expression and cellular transfection. Mol Ther 2005;12:475—83.
[14] De Rosa G, Quaglia F, Bochot A, Ungaro F, Fattal E. Long-term release and improved intracellular penetration of oligonucleotide; polyethylenimine complexes entrapped in biodegradable microspheres. Biomacromolecules 2003;4:529—36.
[15] O'Rorke S, Keeney M, Pandit A. Non-viral polyplexes: scaffold mediated delivery for gene therapy. Prog Polym Sci 2010;35:441—58.

**(b)**

**Fig. 9.** (a) Fluorescent images of hMSC cultured on the scaffolds at day 3 and day 10 stained with Calcein-AM (green) and EthD-1 (red). (b) Cell proliferation ratio calculated by fluorescence images. (*$p < 0.05$). (For interpretation of the references to colour in this figure legend, the reader is referred to the web version of this article.)

## 4. Conclusions

We have prepared PLLA/HA composite scaffolds with different morphology and porosity using TIPS technique. The incorporation of n-HA in dioxane solution has a significant contribution to retard

[16] Nejati E, Mirzadeh H, Zandi M. Synthesis and characterization of nano-hydroxyapatite rods/poly(L-lactide acid) composite scaffolds for bone tissue engineering. Compos Part A 2008;39:1589–96.

[17] Rosa M, Dias R, Miguel MG, Lindman B. DNA-cationic surfactant interactions are different for double- and single-stranded DNA. Biomacromolecules 2005;6:2164–71.

[18] Patil AJ, Li M, Dujardin E, Mann S. Novel bioinorganic nanostructures based on mesolamellar intercalation or single-molecule wrapping of DNA using organoclay building blocks. Nano Lett 2007;7:2660–5.

[19] Hayashi H, Mori T, Okamoto M, Yamasaki S, Hayami H. Polyethylene ionomer-based nano-composite foams prepared by a batch process and MuCell® injection molding. Mater Sci Eng 2010;C30:62–70.

[20] Sakai R, John B, Okamoto M, Seppälä JV, Vaithilingam J, Hussein H, et al. Fabrication of polylactide based biodegradable thermoset scaffolds for tissue engineering applications. Macromol Mater Eng 2013;298:45–52.

[21] Chu B. Laser light scattering: basic principles and practice. 2nd ed. Boston: Academic Press; 1991. p. 343.

[22] Kawachi T, Matsuura Y, Iyoda F, Arakawa S, Okamoto M. Preparation and characterization of DNA/allophane composite hydrogels. Colloids Surfaces B Biointerface 2013;112:429–34.

[23] Bitou M, Okamoto M. Fabrication of porous 3-D structure from poly(L-lactide)-based nano-composite foam via enzymatic degradation. Int Polym Process 2007;22(5):446–54.

[24] Fisher EW, Sterzel HJ, Wegner G. Investigation of the structure of solution growth crystals of lactide copolymers by means of chemical reactions. Kolloid-Z.U.Z. Polym 1973;251:980–90.

[25] Taki A, John B, Arakawa S, Okamoto M. Structure and rheology of nano-composite hydrogels composed of DNA and clay. Eur Polym J 2012;49:923–31.

[26] Freundlich H. Over the adsorption in solution. J Phys Chem 1906;57:385–470.

[27] Schellman JA, Stigter D. Electrical double layer, zeta potential, and electrophoretic charge of double-stranded DNA. Biopolymers 1977;16:1415–34.

[28] Parks GA. Advanced chemistry series, vol. 67. New York: McGraw Hill; 1967. p. 121.

[29] Methods of test for zeta potential of colloids in water and waste water. 1985. ASTM D 4187-82.

[30] Giles CH, MacEwan TH, Nakhwa SN, Smith D. Studies in adsorption. Part XI. A system of classification of solution adsorption isotherms, and its use in diagnosis of adsorption mechanisms and in measurement of specific surface areas of solids. J Chem Soc 1960;148:3973–93.

[31] Ando Y, Sato H, Shinzawa H, Okamoto M, Noda I, Ozaki Y. Isothermal melt crystallization behavior of neat poly(L-lactide) (PLLA) and PLLA/organically modified layered silicate (OMLS) nanocomposite studied by two-dimensional (2D) correlation spectroscopy. Vib Spectrosc 2012;60:158–62.

[32] Brewer SH, Annthireya SJ, Lappi SE, Drapcho DL, Franzen S. Detection of DNA hybridization on gold surfaces by polarization modulation infrared reflection absorption spectroscopy. Langmuir 2002;18:4460–4.

[33] Xiao K, Li Y, Luo J, Lee JS, Xiao W, Gonik AM, et al. The effect on surface on in vivo biodistribution of PEG-oligocholic acid based micellar nanoparticles. Biomaterials 2011;32:3435–46.

[34] Bandar OV, Saifulina DV, Shakhmaeva II, Mavlyutova II, Abdullin TI. Monitoring of the zeta potential of human cells upon reduction in their viability and interaction with polymers. Acta Naturae 2012;4:78–81.

[35] Wilhelm C, Gazeau F, Roger J, Pons JN, Bacri J. Interaction of anionic super-paramagnetic nanoparticles with cells: kinetic analyses of membrane adsorption and subsequent internalization. Langmuir 2002;18:8148–55.

[36] Moghadam BY, Hou W, Corredor C, Westerhoff P, Posner JD. Role of nano-particle surface functionality in the disruption of model cell membrane. Langmuir 2012;28:16318–26.

[37] Wang B, Zhang L, Bae SC, Granick S. Nanoparticle-induced surface recon-struction of phospholipid membranes. Proc Natl Acad Sci U S A 2008;105:18171–5.

[38] Leroueil PR, Berry SA, Duthie K, Han G, Rotello VM, McNerny DQ, et al. Wide varieties of cationic nanoparticles induce defects in supported lipid bilayers. Nano Lett 2008;8:420–4.